Electrochimica Acta 536 (2025) 146805

Contents lists available at ScienceDirect

Electrochimica Acta

journal homepage: www.journals.elsevier.com/electrochimica-acta

A green approach to transition metal-based nanoparticles from aluminium powder cementation for application in OER electrocatalysis

Francesko Malaj [a,b,*], Domenico Lentini [b,c], Alessandro Tampucci [b], Lorenzo Brogi [b], Enrico Berretti [d], Mohsin Muhyuddin [a], Gianluigi Baiardi [e,g], Stiven Forti [e], Antonio Rossi [e], Camilla Coletti [e,f], Oreste Tarallo [c], Francesco Ruffo [c], Carlo Santoro [a,*]

[a] Electrocatalysis and Bioelectrocatalysis Lab, Department of Materials Science, University of Milano-Bicocca, Via Roberto Cozzi 55, Building U5, 20125, Milan, Italy
[b] Ne.m.e.sys. s.r.l., via 2 Giugno 8, 50019 Sesto Fiorentino Fi, Italy
[c] Department of Chemical Sciences, University of Naples Federico II, Complesso Univ. M.S. Angelo, Via Cintia, IT-80126 Naples, Italy
[d] Istituto di Chimica Dei Composti OrganoMetallici (ICCOM), Consiglio Nazionale Delle Ricerche (CNR), Via Madonna Del Piano 10, Sesto Fiorentino, 50019, Firenze, Italy
[e] enter for Nanotechnology Innovation @NEST, Istituto Italiano di Tecnologia, P.zza S. Silvestro 12, 56127, Pisa, Italy
[f] Graphene Labs, Istituto Italiano di Tecnologia, Via Morego 30, 16163 Genova, Italy
[g] NEST laboratory, Scuola Normale Superiore, P.zza S. Silvestro 12, 56127 Pisa, Italy

ARTICLE INFO

Keywords:
AEM water electrolyzers
Platinum group metal-free
Aluminum powder cementation
OER electrocatalysts

ABSTRACT

Anion-exchange-membrane water electrolyzers (AEMWEs) represent a highly promising technology for hydrogen production using renewable energy sources. To enable the broad implementation of AEMWEs, it is crucial to improve simple, scalable and environmentally friendly synthetic methods for the development of transition metal-based electrocatalysts. Here, $FeCo_3/FeCoO_x$ and $Ni_{1-x}Co_x/NiCoO_x$ nanoparticles were obtained via a feasible two-step synthesis in an aqueous solution by cementation of aluminium powder. Both materials were tested as oxygen evolution reaction (OER) electrocatalysts comparing the electrochemical performance with commercial benchmark RuO_2. The $FeCo_3/FeCoO_x$ and $Ni_{1-x}Co_x/NiCoO_x$ exhibited overpotentials of 288 mV and 296 mV, respectively, for OER at a current density of 10 mA cm^{-2}, allowing a comparison between mass activity and geometric activity with RuO_2. When integrated as anode electrocatalyst into a pilot-scale AEMWE, the materials were able to reach 2.10 V and 2.24 V (without iR-correction) at a current density of 1 A cm^{-2} (50 °C), respectively. After acquiring the polarization curves, the AEMWE tests were extended for 100 h with a continuous power profile, to have an initial assessment of the possible degradation trends for a future industrial application. The degradation rate resulted in 396 μV h^{-1} in the case of $FeCo_3/FeCoO_x$ and no significant degradation for $Ni_{1-x}Co_x/NiCoO_x$. This study presents a straightforward and scalable approach to synthesizing earth-abundant electrocatalytic materials designed for high-efficiency OER.

1. Introduction

Hydrogen produced by renewable energy sources can be used as an energy vector and reconverted into electricity on demand [1,2]. Anion-exchange-membrane water electrolysis (AEMWE) is a promising technology for large-scale hydrogen production that can be easily coupled to discontinuous energy sources and, thanks to the use of an alkaline environment, it allows the use of abundant and inexpensive materials (i.e. first row transition metals) [3–5]. During water electrolysis in alkaline environment, the oxidative half-reaction is the oxygen evolution reaction (OER) occurring at the anode, which exhibits slow kinetics due to its mechanism involving a four-electron process [6,7]. In view of the widespread deployment of AEMWEs, the use of electrocatalysts that lower the overpotential for the OER is essential to increase its efficiency [8]. Although ruthenium oxide (RuO_2) and iridium oxide (IrO_2) are widely used as benchmark electrocatalysts for OER in alkaline media due to their high performance, their intrinsic disadvantages, such as low abundance and high cost, greatly limit their industrial application [9–11]. In recent years, considerable efforts have been made to find high-performance and durable OER electrocatalysts based on first row

* Corresponding authors.
E-mail addresses: f.malaj@campus.unimib.it (F. Malaj), carlo.santoro@unimib.it (C. Santoro).

https://doi.org/10.1016/j.electacta.2025.146805
Received 3 March 2025; Received in revised form 18 June 2025; Accepted 29 June 2025
Available online 30 June 2025

transition (TMs), with the most promising ones being nickel, iron and cobalt [12–14]. In particular, the synthesis of nanomaterials based on alloys of these TMs can lead to simple and active electrocatalysts. In our previous work, we synthesized nanoparticles based on $FeNi_3$ alloys through chemical reduction using hydrazine which showed an overpotential of 234 mV for OER at 10 mA cm^{-2} [15]. Lu et al. formed nanospheres based on $FeCo_4$ alloy by the electrodeposition method, resulting in overpotentials of 275 mV at 10 mA cm^{-2} [16]. Yang et al. obtained CoFe alloy-based nanoparticles via sol-gel self-propagating combustion method followed by a reduction in controlled atmosphere which exhibited an overpotential of 310 mV at 10 mA cm^{-2} [17]. Zhang et al. described the synthesis of NiCo nanochain arrays with thin oxide coating by one-step low-temperature reduction of $NiCo_2O_4$ nanorod arrays in H_2/Ar and the resultant material showed an overpotential of 320 mV at 10 mA cm^{-2} [18]. Given the good performance achieved so far by these TM-based alloys, it is important to develop synthesis methods that are environmentally friendly, economical and scalable. The reduction of metal ions on the surface of a less noble metal (i.e. cementation) is a practical strategy used in industry for metal recovery and purification of solutions containing metal ions [19–21]. Recently, this technique was proven to be a good synthetic strategy for obtaining nanoparticles [22–24]. Aluminium appears to be particularly interesting for this type of application due to its high reducing power, eco-sustainability and low cost but, despite its potential, it remains an unexplored element for the synthesis of nanoparticles that can be used as electrocatalysts for water splitting [25,26]. Here, we report the synthesis and characterization of $FeCo_3/FeCoO_x$ and $Ni_{1-x}Co_x/NiCoO_x$ nanoparticles and their use as OER electrocatalyst. The synthetic design was inspired by the aim of combining various beneficial aspects of green chemistry, such as the use of harmless solvents, the reduction of undesirable by-products and auxiliary substances, the adoption of mild and easily scalable reaction conditions, as well as the selection of cost-effective and widely available raw sources. The materials were obtained via a feasible two-step synthesis in aqueous solution using aluminium powder as a reducing agent, with subsequent removal by alkaline treatment. These nanoparticles were characterized by means of high-resolution transmission electron microscopy (HRTEM), high-angle annular dark field scanning transmission electron microscopy (HAADF-STEM), X-ray photoelectron spectroscopy (XPS), X-ray diffraction (XRD), X-ray fluorescence (XRF), and scanning electron microscope (SEM). The materials were electrochemically characterized by linear sweep voltammetry (LSV), electrochemical impedance spectroscopy (EIS) and used as OER electrocatalyst in a pilot-scale AEMWE with a 50 cm^2 of geometric active area. The $FeCo_3/FeCoO_x$ and $Ni_{1-x}Co_x/NiCoO_x$ nanoparticles electrocatalysts demonstrated overpotentials of 288 mV and 296 mV, respectively, for OER at a current density of 10 mA cm^{-2} when tested as single electrodes. These materials were able to operate at voltages of 2.10 V and 2.24 V, respectively, when integrated into AEMWE at current densities of 1 A cm^{-2}, at operating temperature of 50 °C. These results were also compared with those of the commercial benchmark RuO_2, and both PGM-free nanoparticles outperformed it in all the electrochemical tests conducted. Additionally, 100 h continuous stability tests when integrated into AEMWE were conducted to observe the degradation trends of both electrocatalysts, resulting in no significant degradation for $Ni_{1-x}Co_x/NiCoO_x$ and 396 μV h^{-1} for $FeCo_3/FeCoO_x$.

2. Materials and methods

2.1. Reagents

Iron(II) chloride tetrahydrate ($FeCl_2 \cdot 4\ H_2O$), nickel(II) chloride hexahydrate ($NiCl_2$ 0·6 H_2O), cobalt(II) chloride hexahydrate ($CoCl_2$ 0·6 H_2O), ruthenium(IV) oxide (RuO_2, 99.9 % metals basis), ethanol, polyvinyl Alcohol (Mw 89,000–98,000, 99 % hydrolyzed), polytetrafluoroethylene 60 wt % dispersion in H_2O, sodium hydroxide (NaOH, 98 %), and potassium hydroxide (KOH, purity 85 %) were purchased from Sigma-Aldrich and used as received without further purification.

Aluminum powder (Al, 325 mesh, 99.5 %) and platinum supported on carbon (Pt/C, 40 wt %) were purchased from Thermo Scientific and used as received without further purification.

Carbon cloth porous transport layer (0.410 mm thickness, Xiamen Zopin New Material Limited, China); Nickel foam (1.5 mm, Xiamen Tmax Battery Equipments Limited, China).

The binder (Ethanolic solution 10 % w/v) and the anion exchange membranes (AEMs) utilized in the study (AT-100) were kindly supplied by Ne.m.e.sys. s.r.l. (Italy).

2.2. Synthesis

First step: $FeCo_3/FeCoO_x$ and $Ni_{1-x}Co_x/NiCoO_x$ nanoparticles (NPs) were synthesized through a wet chemical reduction method using the same procedures. In the case of $FeCo_3/FeCoO_x$, 5 g of $CoCl_2$ 0·6 H_2O (21 mmol) and 1.0 g of $FeCl_2$ 0·4 H_2O (5 mmol) were dissolved in 50 ml of water; in the case of $Ni_{1-x}Co_x/NiCoO_x$, 5 g of $NiCl_2$ 0·6 H_2O (21 mmol) and 1.0 g of $CoCl_2$ 0·4 H_2O (4.2 mmol) were dissolved in 50 ml of water. The mixtures were stirred for 5 min and then heated to reach 90 °C. 5.0 g of aluminium powder was added to the solution, and within a few minutes, an exothermic reaction was observed, along with the formation of gas. The reaction was kept at 90 °C until complete evaporation of the water. The nanoparticles were magnetically fixed to one side of the vessel and abundantly washed with water.

Second step: In order to detach NPs from the surface of the aluminium particles, the powders were dispersed in 100 mL of water at room temperature and then 8 g of NaOH was added. After the evolution of gas ceased, the washing procedure was carried out in five cycles with portions of running water, followed by five additional washes with ethanol. During each step, nanoparticles were initially freely dispersed and subsequently magnetically decanted between washes, in order to remove non-magnetically active particles with the washing liquids. After the final ethanol wash, the particles were filtered, and recovered.

2.4. Preparation of electrode

2.4.1. Preparation of the standard electrodes

The benchmark electrocatalysts selected for the given study were RuO_2 for the OER and Pt/C for the HER [27]. The electrode for the three-electrode measurement system was manufactured as follows: 24 mg of RuO_2 powder was dispersed in 54 μL of the binder ethanolic solution. The ink was spread onto 6 cm^2 of nickel foam and dried in an oven overnight at 30 °C. The final electrocatalyst loading, confirmed by monitoring the weight difference between the pristine and loaded nickel foam, was 4 mg cm^{-2}.

The anode electrode for the AEMWE cell test was manufactured as follows: 200 mg of RuO_2 powder was dispersed in 448 μL of the binder ethanolic solution. The ink was spread onto 50 cm^2 of nickel foam and dried in an oven overnight at 30 °C. The final electrocatalyst loading, confirmed by monitoring the weight difference between the pristine and loaded nickel foam, was 4 mg cm^{-2}.

The cathode electrode for the AEMWE cell test was manufactured as follows: 62.5 mg of Pt/C powder was mixed, in an ultrasonic bath for 30 min, to 140 μL of a 10 % w/v aqueous solution of polyvinyl alcohol. The ink was spread onto 50 cm^2 of carbon cloth used as a porous transport layer (PTL) and dried in an oven overnight at 50 °C. The final Pt loading, confirmed by monitoring the weight difference between the pristine and loaded carbon cloth, was 0.5 mg cm^{-2}.

2.4.2. Preparation of the $FeCo_3/FeCoO_x$ electrode

The electrode for the three-electrode measurement system was manufactured as follows: 150 mg of $FeCo_3/FeCoO_x$ powder was dispersed in 800 μL of ethanol and 27 mg of the aqueous dispersion of Polytetrafluoroethylene (60 wt %) was added. The ink was manually

spread onto 6 cm^2 of nickel foam and dried in an oven overnight at 30 °C. The final electrocatalyst loading, confirmed by monitoring the weight difference between the pristine and loaded nickel foam, was 25 mg cm^{-2}.

The anode electrode for the AEMWE cell test was manufactured as follows: 1.25 g of $FeCo_3/FeCoO_x$ powder was dispersed in 5 mL of ethanol and 0.230 g of the aqueous dispersion of Polytetrafluoroethylene (60 wt %) were added. The ink was manually spread onto 50 cm^2 of nickel foam and dried in an oven overnight at 30 °C. The final electrocatalyst loading, confirmed by monitoring the weight difference between the pristine and loaded nickel foam, was 25 mg cm^{-2}.

2.4.3. Preparation of the $Ni_{1-x}Co_x/NiCoO_x$ electrode

The electrode for the three-electrode measurement system was manufactured as follows: 150 mg of $Ni_{1-x}Co_x/NiCoO_x$ powder were dispersed in 800 μL of ethanol and 27 mg of the aqueous dispersion of Polytetrafluoroethylene (60 wt %) were added. The ink was manually spread onto 6 cm^2 of nickel foam and dried in an oven overnight at 30 °C. The final electrocatalyst loading, confirmed by monitoring the weight difference between the pristine and loaded nickel foam, was 25 mg cm^{-2}.

The anode electrode for the AEMWE cell test was manufactured as follows: 1.25 g of $Ni_{1-x}Co_x/NiCoO_x$ powder was dispersed in 5 mL of ethanol and 0.230 g of the aqueous dispersion of Polytetrafluoroethylene (60 wt %) were added. The ink was manually spread onto 50 cm^2 of nickel foam and dried in an oven overnight at 30 °C. The final electrocatalyst loading, confirmed by monitoring the weight difference between the pristine and loaded nickel foam, was 25 mg cm^{-2}.

2.5. Electrochemical measurements

The OER tests were conducted with a Biologic VSP potentiostat/galvanostat (France) equipped with (EIS) and an Arbin BT-G battery testing workstation (USA) in a three-electrode system, using a reversible hydrogen electrode (RHE) Mini HydroFlex 80,521 (Gaskatel, Germany) as the reference.

LSV curves were obtained by applying a scan rate of 5 mV s^{-1} under continuous stirring at 600 rpm to prevent gas bubble accumulation on the electrodes at room temperature. Prior to recording the LSV curves, electrode activation was performed through CV in a potential window ranging from 1.2 V to 1.8 V vs RHE for OER until a stable CV was achieved. Electrocatalyst overpotentials were determined from the recorded LSV curves at a current density of 10 mA cm^{-2}. EIS was performed at 1.55 V vs. RHE over a frequency range from 100 mHz to 100 kHz with an AC amplitude of 15 mV.

Overall water electrolysis tests were carried out in a single-cell AEMWE with an active area of 50 cm^2 (SCBT-100, Nemesys S.r.l.). The cell assembly consisted, in order, of a stainless-steel end plate, a bipolar plate (connected to the positive terminal), a plastic frame and an end plate (connected to the negative terminal). The plastic frame has a channel responsible for the flow of electrolyte and house the positive electrode (Nickel foam loaded with catalyst), the anion-exchange membrane and the negative electrode (catalyzed carbon cloth). The entire stack was held together by stainless-steel bolts, which compressed the assembly between the end plates at a pressure of approximately 2 MPa.

The performances of the electrocatalysts developed in this study have been compared to RuO_2 as OER on the anode, through the acquisition of polarization curves at 50 °C.

The MEA was formed by mechanical compression of the AT-100 membrane (Nemesys s.r.l.) sandwiched between the anode and cathode at a pressure of 2 MPa. The membrane was previously activated in a 1 M KOH aqueous solution for 24 h reaching a thickness of 60 μm. Electrodes were previously activated in a 1 M KOH aqueous solution for 30 min. The electrolyte was 1 M KOH aqueous solution supplied by a peristaltic pump with a flow rate of 200 mL/min.

Polarization curves were obtained by applying current steps while voltages were measured on-line by Hioki 3560 AC mW HiTester (Hioki Corporation, Japan).

Finally, an analysis of the degradation trend of the $FeCo_3/FeCoO_x$ and $Ni_{1-x}Co_x/NiCoO_x$.based MEAs in continuous power supply was conducted. The tests were performed at a current density of 0.4 A cm^{-2}, at 50 °C for 100 h. All electrochemical measurements were conducted in 1 M KOH as a supporting electrolyte.

2.6. Characterization methods

2.6.1. XPS analysis

X-Ray photoelectron spectroscopy (XPS) measurements were carried out using a Specs XR50 source with an Al anode at a power of 300 W. The analyzer employed was a Specs Astraios 190 with a 2D-CMOS detector and a 3 × 25 mm entrance slit. All spectra were acquired with a pass energy of 10 eV, in normal emission conditions. The binding energies of the spectra have been referenced to the position of the adventitious carbon C 1 s at 285.2 eV.

All spectra were fitted first by iteratively calculating a Shirley background and then using a linear combination of (i) symmetric Gaussian-Lorentzian sum (GLS) single peaks (or doublets) for all signals related to oxidized states and their satellites, and (ii) asymmetric Lorentzian single peaks (or doublets) for Auger lines and signal related to metallic states. The components are explicitly shown in the plots and described in the legends, together with the resulting envelope function.

2.6.2. XRD analysis

Wide angle X-ray diffraction (XRD) patterns were collected in the 2θ range of 10–90° by using a Rigaku Miniflex 600 equipped with a copper source.

2.6.3. XRF analysis

Inorganic elemental analysis was qualitatively carried out using X-rays fluorescence (XRF) (Artax 200, Bruker, Billerica, MA, USA) having Mo anode.

2.6.4. SEM analysis

For the morphological analysis of the electrocatalyst, a desktop scanning electron microscope (SEM) (Thermo Fisher Phenom G6, Eindhoven, The Netherlands) equipped with a thermionic CeB6 source was employed. The instrument operates in the magnification range of 400–70000x.

2.6.5. HRTEM analysis

High-resolution transmission electron microscope (HRTEM) images were acquired using a Thermofisher Talos F200X G2 at an accelerating voltage of 200 kV using a high-speed CETA camera operating at a camera resolution of 4096 × 4096 pixels without any objective aperture. The High-Angle Annular Dark Field images were acquired with a Panther annular STEM detector using a convergent beam with an angle of 10.5 mrad and a camera length of 330 mm. The EDX maps were taken with a Super X spectrometer equipped with four 30 mm^2 silicon drift detectors with a collection angle of 0.7 srad.

3. Results and discussion

3.1. Synthesis and characterization

Cementation refers to a chemical and physical process in which metal ions in a solution are reduced and deposited on the surface of a less noble metal. Given the standard redox potential of Al^{3+}/Al (−1.66 V), Fe^{2+}/Fe (−0.44 V), Co^{2+}/Co (−0.28 V), and Ni^{2+}/Ni (−0.25 V), theoretically, metallic aluminium is forced to oxidize and the metal ions are reduced to their zero-valent metallic state, eventually forming an alloy. In practice, although the redox nature of aluminium makes it an

excellent reducing agent for wet chemical synthesis, on its surfaces a non-conductive oxide layer of a few nanometres is rapidly formed (3×10^{-9} s) even in water, which limits its applications, especially at pH≈7 [28]. The selection of metal salts having chlorides as counterions is convenient because, as reported by McCafferty, they favor the pitting phenomenon allowing the use of aluminium powder as a reductant even in neutral aqueous solutions. It has been hypothesized that, at these pH values, the oxide layer carries a positive charge, which attracts chloride ions. These ions adsorb onto the surface and penetrate the oxide layer until they reach the underlying zero-valent aluminum. There, the combined action of water (present within the oxide layer) and chloride ions promotes aluminum oxidation and dissolution, creating a localized acidic environment. This process releases electrons and prevents the rapid reformation of the oxide layer. As a result, gaseous hydrogen evolves, contributing to the pitting corrosion phenomenon. An intermediate step in this process involves the formation of hydrogen radicals, which diffuse through the oxide layer to the surface, where they reduce metal cations, leading to the formation of nanoparticles [26,28]. The SEM images in Fig. 1a and Fig. 1b show the pristine aluminium powder; Fig. 1c and d show the growth of $FeCo_3/FeCoO_x$ and $Ni_{1-x}Co_x/NiCoO_x$ respectively on the surface of the aluminium powder (before treatment with NaOH).

During the second reaction step, the particles are dispersed in an aqueous solution and then NaOH is added to make the solution highly alkaline. The highly concentrated hydroxide ions reactwith the oxide layer exposed on aluminium (where no NPs have been grown) forming soluble aluminate ions and causing the exposure of zero-valent metal. The contact between the aluminium and the alkaline solution causes an exothermic redox reaction to occur, with gas development (eq. 1):

$$2\ Al_{(s)} + 6\ H_2O_{(l)} + 2\ OH^-_{(aq)} \rightarrow 2\ [Al(OH)_4]^-_{(aq)} + 3\ H_{2(g)} \quad (1)$$

Fig. 1e and f show the NPs aggregates obtained after treatment with the alkaline solution. In both reaction steps gas is produced simultaneously with the formation of a fine black powder. Despite the complex reaction mechanism, from a macroscopic point of view, the reactions are not very complex to implement, require a simple experimental set-up and are completed in a few minutes followed by a rapid work-up (filtering and drying). The molar ratios used were chosen arbitrarily in order to verify the effectiveness of the reaction process in giving nanoparticles based on Ni/Co and Fe/Co alloys, already demonstrated to be active as OER electrocatalysts. The XRF analysis was done to confirm the presence of the metal of interest. (Figure S1, Figure S2, Supporting Information). The $Ni_{1-x}Co_x/NiCoO_x$ spectrum also reveals a slight spot attributable to the presence of iron, probably due to impurities in the reagents. The XRD pattern of $Ni_{1-x}Co_x/NiCoO_x$ (Fig. 2a) displays three peaks at 2θ= 44.5°, 51.9°, and 76.4°, corresponding at the crystallographic plane family (111), (002) and (022) respectively of metallic nickel (JCPDS Card No 96–210–0662). The XRD pattern of $FeCo_3/FeCoO_x$ (Fig. 2b) displays three peaks at 2θ=45.3°, 65.9°, and 83.5°, corresponding at the crystallographic plane family (011), (020) and (121) respectively of $FeCo_3$ alloy (JCPDS Card No 96–152–4168).

HRTEM coupled with EDX analysis for both NPs are shown in Figs. 3 and 4. The presence of the expected metals, together with oxygen, was confirmed by EDX analyses, as well as a lattice spacing of 0.203 nm corresponding to the 111 faces of metallic nickel in the case of $Ni_{1-x}Co_x/NiCoO_x$ and a lattice spacing of 0.199 nm corresponding to the 111 faces of the $FeCo_3$ alloy in the case of $FeCo_3/FeCoO_x$, in agreement with the result of XRD. The average size and shape of the nanoparticles were not uniformly distributed. For both materials, EDX revealed residual amounts of aluminum within the nanoparticle matrix, presumably in the form of amorphous oxide, with an average atomic fraction below 0.5 %.

For $Ni_{1-x}Co_x/NiCoO_x$, from the HAADF-STEM analysis (Fig. 5a) of three different nanoparticles, we can approximate an average molar ratio of nickel, cobalt and oxygen within the nanoparticles equal to 7:1:6 respectively. For $FeCo_3/FeCoO_x$, from the same analysis methods (Fig. 5b), we can approximate an average molar ratio of cobalt, iron and oxygen within the nanoparticles equal to 5:1:2 respectively. Using these stoichiometric ratios in the products it is possible to calculate the yield of the reactions by comparing, for three different batches, the weight of the metal salts to the weight of the final washed and dried powder (after the second step). From the results shown in Table S1 and Table S2, it is possible to approximate a reaction yield of 62 % for the $Ni_{1-x}Co_x/NiCoO_x$ and 95 % for the $FeCo_3/FeCoO_x$.

Fig. 6 reports on the XPS high-resolution scans in the 2p-core-level energy range of the transition metals of interest in each case: nickel and cobalt for $Ni_{1-x}Co_x/NiCoO_x$ (Fig. 6a and b), iron and cobalt for $FeCo_3/FeCoO_x$ (Fig. 6c and d). The different intensities (i.e. signal-to-noise ratios) suggest that Ni dominates the composition of $Ni_{1-x}Co_x/$

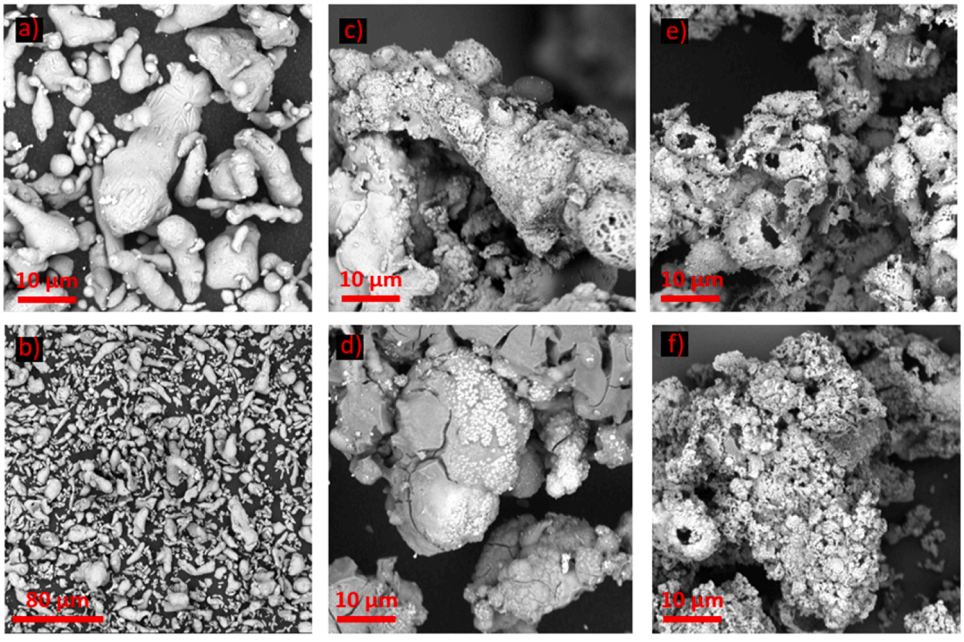

Fig. 1. SEM images at different magnification of: (a) and (b) pristine aluminium powder; (c) $FeCo_3/FeCoO_x$ calcinated on aluminium powder; (d) $Ni_{1-x}Co_x/NiCoO_x$ calcinated on aluminium powder; (e) $FeCo_3/FeCoO_x$ aggregate; (f) $Ni_{1-x}Co_x/NiCoO_x$ aggregate.

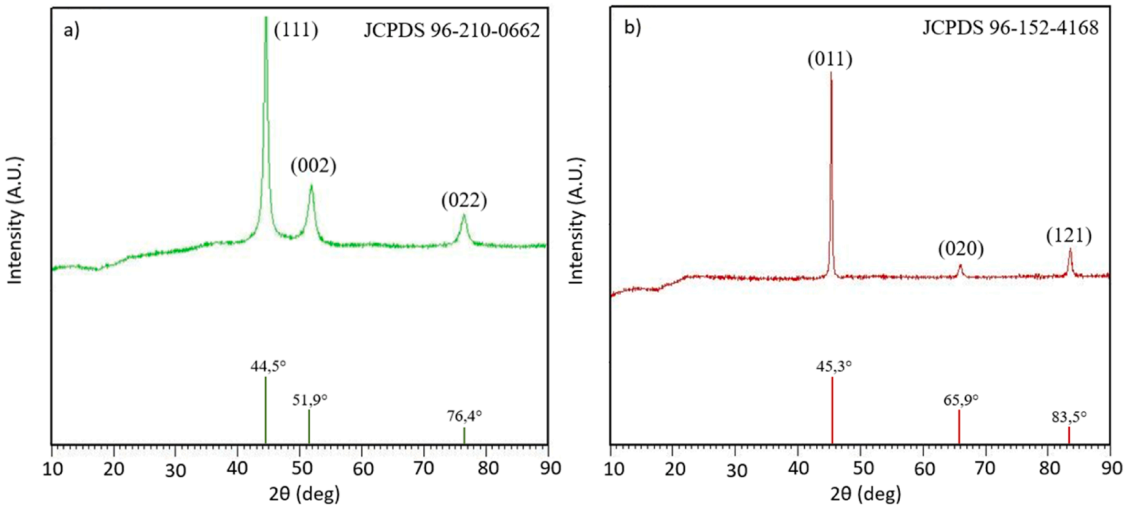

Fig. 2. XRD diffraction patterns of (a) $Ni_{1-x}Co_x/NiCoO_x$ and (b) $FeCo_3/FeCoO_x$ powders.

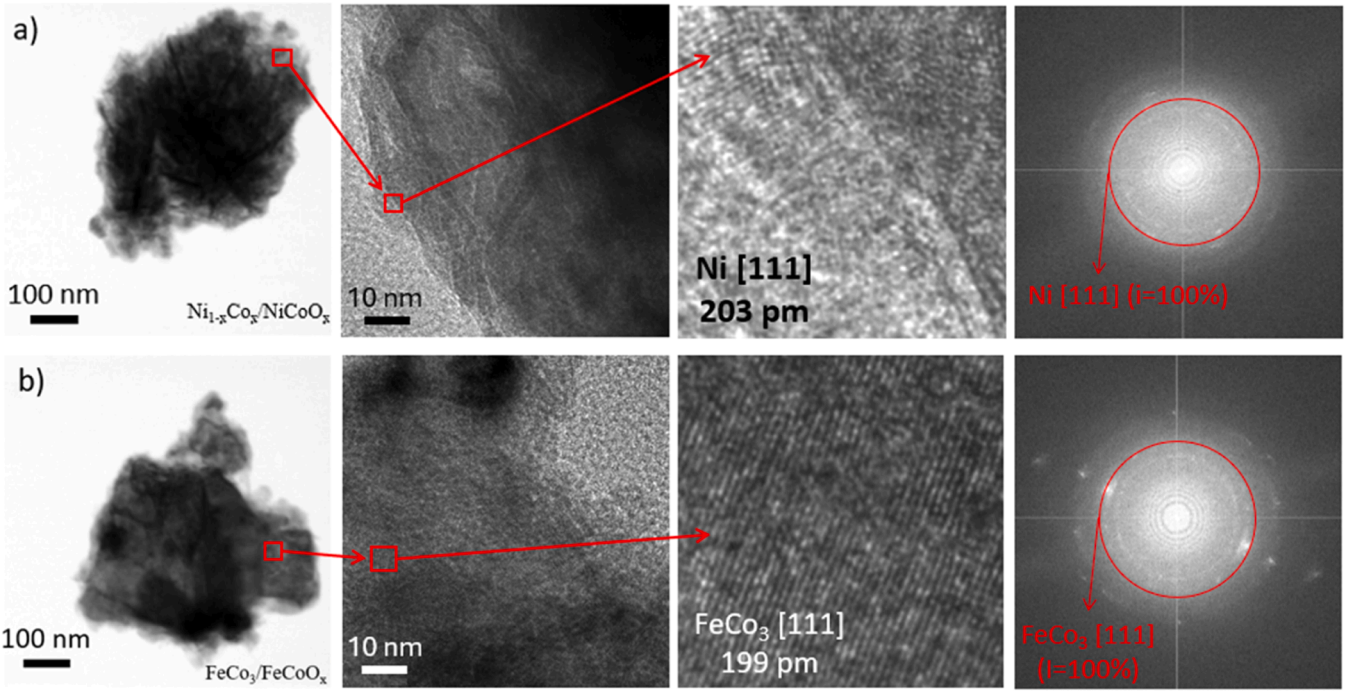

Fig. 3. HR-TEM image for (a) $Ni_{1-x}Co_x/NiCoO_x$ and (b) $FeCo_3/FeCoO_x$.

$NiCoO_x$, while Co that of $FeCo_3/FeCoO_x$, at least when considering the surface of the particle. In particular, the Fe 2p signal we recorded from the $FeCo_3/FeCoO_x$ powder, suggests that in the first few nanometers of depth in the particles (i.e. the probing depth of the technique), iron amounts to a negligible quantity, as the spectrum in the region can be fully attributed to the $L_{2,3}VV$ Auger lines of Co [29,30] (Figure S3, Supperting Information). Concerning the shape and relevant binding energies of the data, all the remaining three scans (two Co 2p and one Ni 2p) can be associated with oxidized states of the metals, given the position and large FWHM of the main peaks and the presence of strong shake-up satellites, which is coherent with the detection of oxygen by EDX. The broadening of the signal due to the powdery nature of the system and to its chemical complexity, however, does not allow to further resolve all the components and determine the identity of the oxidized compounds (e.g., whether they are simple oxides or hydroxides and the precise oxidation number of the metallic elements). However, it appears clear that both powders are completely oxidized, at least at their surface, in full agreement with the EDX data reported in Fig. 3. In Fig. 6a, the metallic Ni component appears as a shoulder on the right of the main peak, leading to an estimation of its atomic percentage of about 10 % out of all detected Ni. The broad feature at low binding energies in Fig. 6b could be assigned to a Co/Ni intermetallic, which amounts to roughly 40 at %, while Co oxides and hydroxides constitute the remaining 60 at %. In Fig. 6d, instead, we can distinguish the components associated to Co(III), or $Co(OH)_2$, and its first satellite, with binding energy and spin doublet separation in strong agreement with the literature [31]. Here, the Co(0) signal suggests approximatively 5 at % of metallic Co against 95 at % of Co(III)/$Co(OH)_2$. An iterated Shirley background was computed in all cases, including also the signal from the non-fitted $J = 1/2$ region in Fig. 6b Standard doublet constraints were enforced. All Auger and metal-state lineshapes are asymmetric Lorentzian functions, whereas the remaining, associated with oxidized

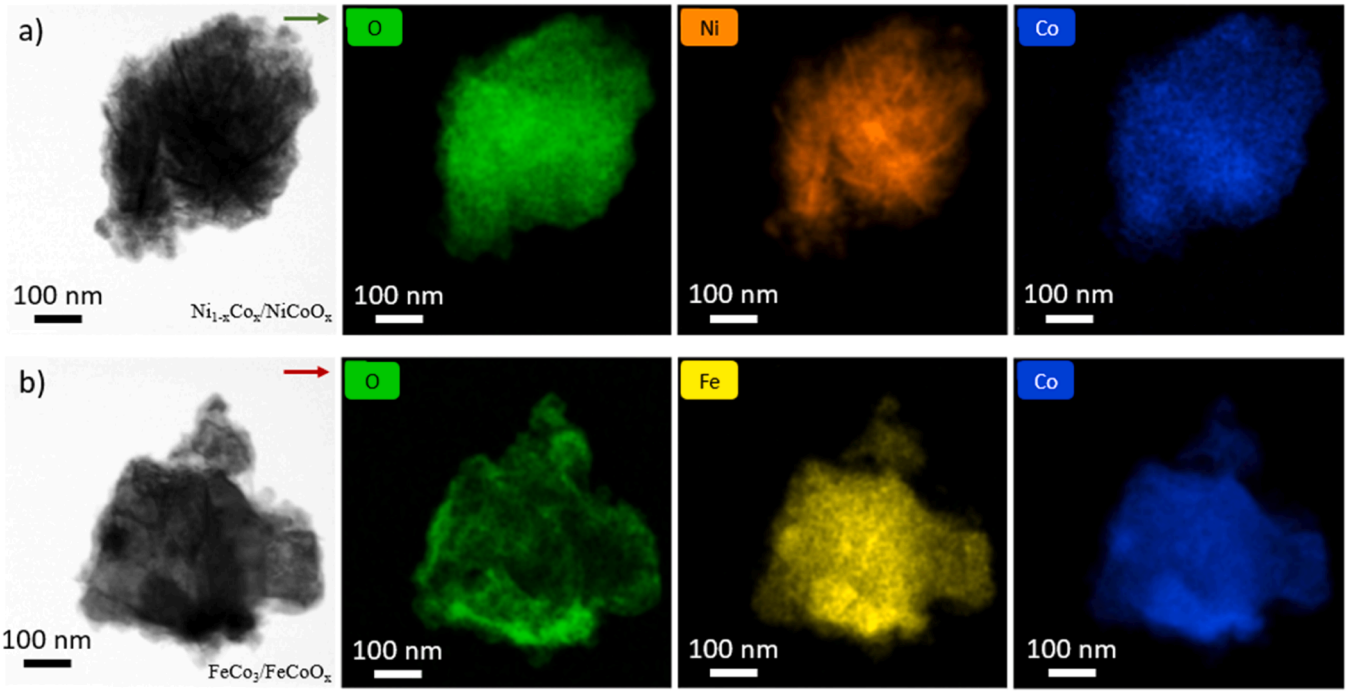

Fig. 4. HR-TEM image with EDX mapping for (a) $Ni_{1-x}Co_x/NiCoO_x$ and (b) $FeCo_3/FeCoO_x$.

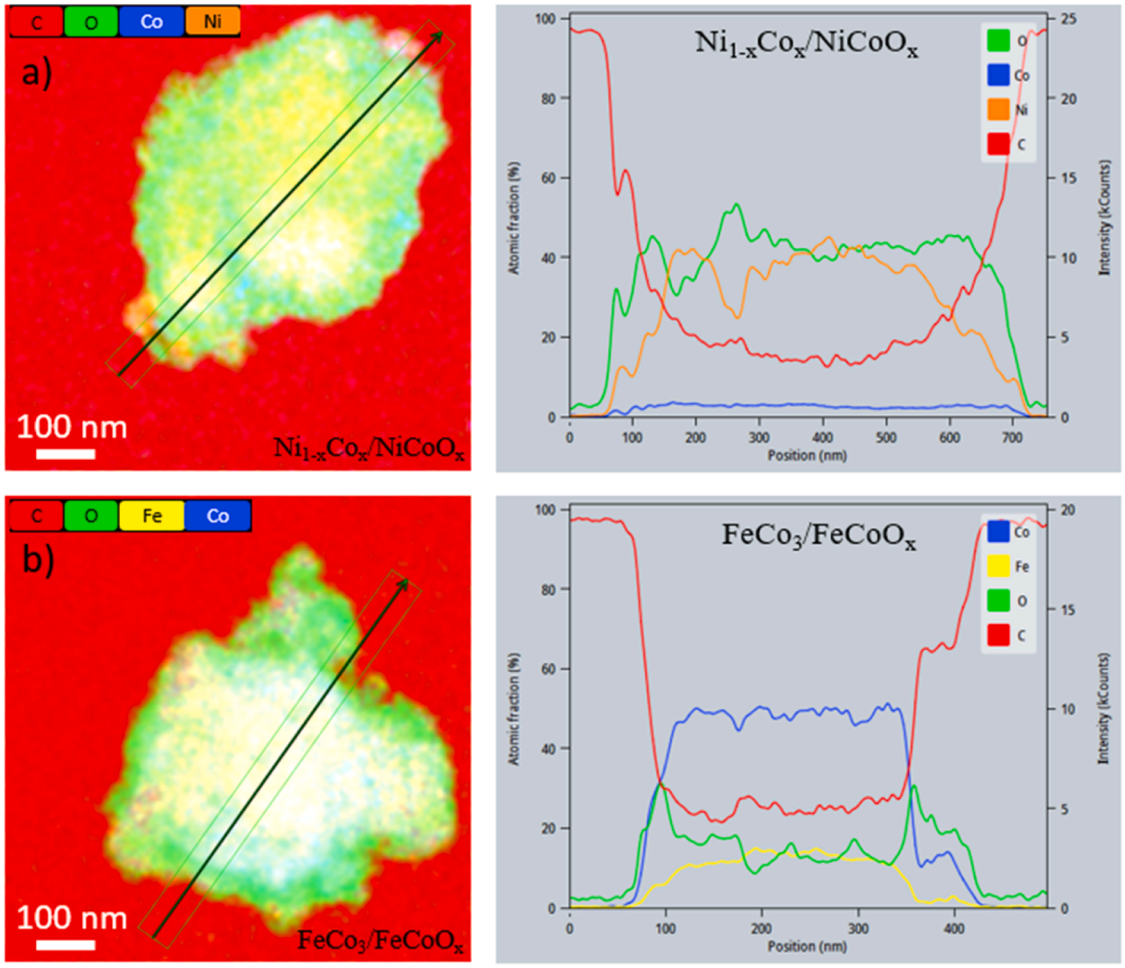

Fig. 5. HAADF-STEM of (a) $Ni_{1-x}Co_x/NiCoO_x$ and (b) $FeCo_3/FeCoO_x$ and the relative atomic fraction of the elements.

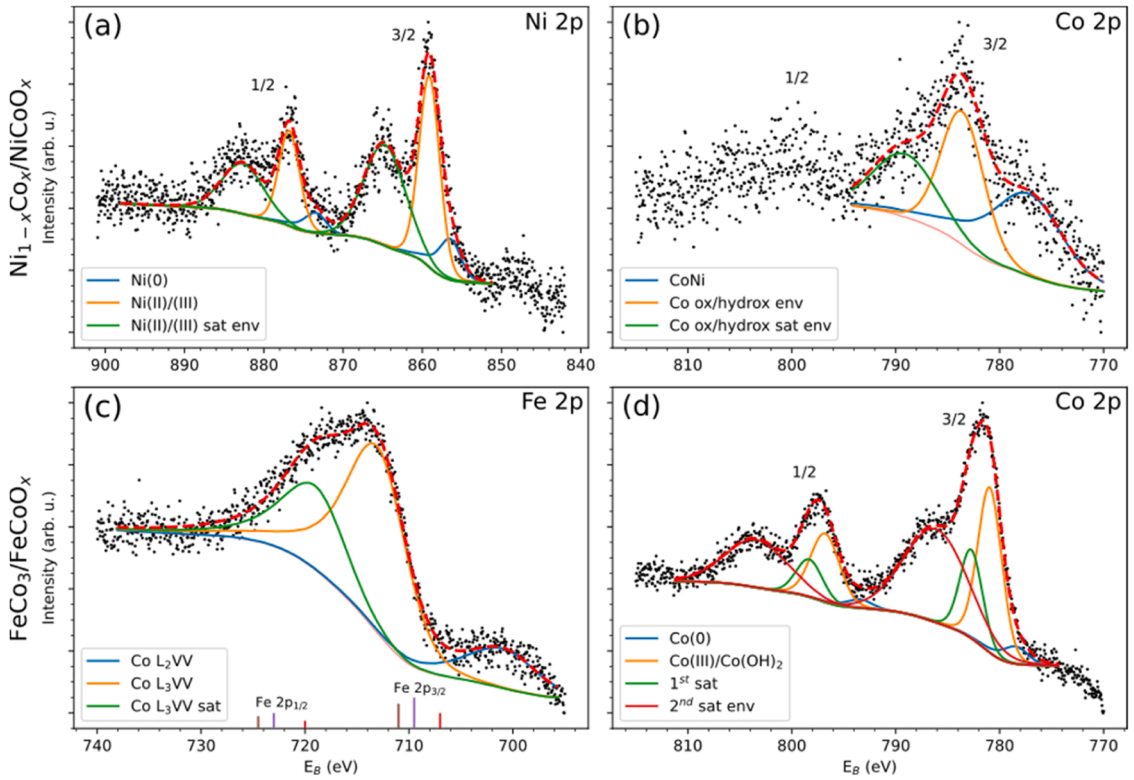

Fig. 6. XPS narrow scans of 2p binding energy ranges of (a) Ni and (b) Co from $Ni_{1-x}Co_x/NiCoO_x$ and of (c) Fe and (d) Co from $FeCo_3/FeCoO_x$. The doublets reported at the bottom of panel (c) represent the expected contribution of (mainly oxidized) Fe 2p levels.

states, are symmetric Gaussian-Lorentz sums. "sat" refers to the shake-up satellites, "env" denotes that the component is the envelope of non-resolvable multiplets.

Due to the simultaneous presence of the alloys and higher oxidation states of the metals both in the core and on the surface, the obtained nanoparticles were renamed as $Ni_{1-x}Co_x/NiCoO_x$ and $FeCo_3/FeCoO_x$.

3.2. Electrochemical activity toward OER reaction

The electrocatalytic activity of the materials obtained for OER was firstly investigated in a standard three-electrode system choosing commercial RuO_2 as the benchmark electrocatalyst and electrochemically evaluated under the same conditions for comparison, using 1 M KOH as electrolyte. The $Ni_{1-x}Co_x/NiCoO_x$ and $FeCo_3/FeCoO_x$ loading onto the nickel foam were the same for every set-up, as reported previously in Materials and Methods Section. SEM images of the electrode (Figure S4, Figure S5, Supporting information) demonstrates the complete coverage of the PTL, which can be attributed to the high compatibility between the binder and the electrocatalyst. This compatibility enables the formation of a uniform mixture and ensures effective adhesion to the surface. When observed at higher magnification, the same electrodes exhibit fractures, roughness, and inhomogeneity. These characteristics are beneficial as they increase the surface area, enhancing mass transfer and the release of gaseous products from the electrode, thereby promoting the OER [32]. Information about overpotentials and the kinetics were obtained thanks to LSV (Fig. 7a) and Tafel slopes analysis (Fig. 7b). $FeCo_3/FeCoO_x$ nanoparticles demonstrated higher OER activity with an overpotential of 288 mV at the benchmark current density of 10 mA cm^{-2}. At the same current density, $Ni_{1-x}Co_x/NiCoO_x$ and RuO_2 showed overpotentials of 296 mV and 323 mV respectively. This trend was confirmed by the Tafel slopes: $FeCo_3/FeCoO_x$ has a lower slope, 34.5 mV dec^{-1}, than that of $Ni_{1-x}Co_x/NiCoO_x$, 50.5 mV dec^{-1}, both with higher kinetics compared to RuO_2, 53.7 mV dec^{-1}. These results are in line with the literature Table 1.

An evaluation of the charge transfer resistances (R_{CT}) was conducted by the acquisition of the Nyquist plots, fitted by an equivalent circuit

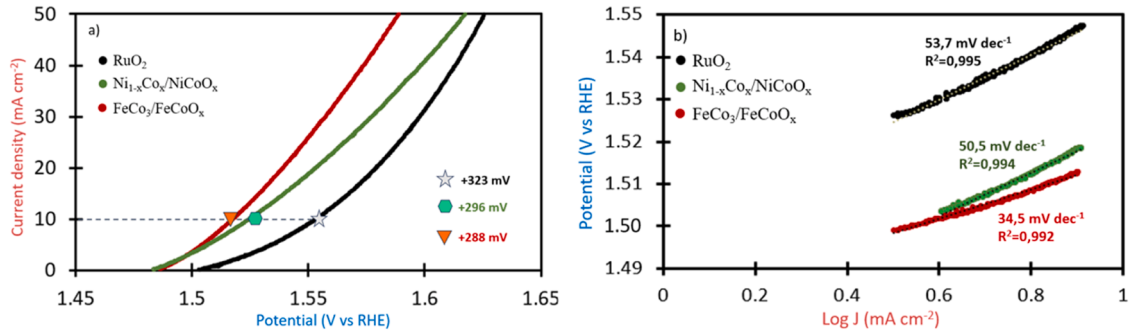

Fig. 7. (a) LSV comparison of OER electrocatalysts in 1.0 M KOH solution at a sweep rate of 5 mV s^{-1}: $FeCo_3/FeCoO_x$ (red curve), $Ni_{1-x}Co_x/NiCoO_x$ (green curve), RuO_2 (black curve). (b) Tafel Plot comparison of OER electrocatalysts: $FeCo_3/FeCoO_x$ (red curve), $Ni_{1-x}Co_x/NiCoO_x$ (green curve), RuO_2 (black curve).

Table 1
Comparison of overpotentials at 10 mA cm^{-2} and Tafel slopes among of OER catalysts.

OER catalyst	Overpotential (mV at 10 mA cm^{-2})	Tafel slope (mV dec^{-1})	Electrolyte (KOH)	Ref.
$Ni_{1-x}Co_x/NiCoO_x$	296	50.5	1M	This work
$FeCo_3/FeCoO_x$	288	34.5	1M	This work
NiCo-$NiCoO_x$ with oxide layer	389	74	1M	[33]
NiCo with oxide layer	287	39	1M	[33]
$Ni_xCo_{3-x}O_4$/NF	287	88	0.1M	[34]
$NiCoO_x$-400	280	74	1M	[35]
$Co_3Fe_{1.5}$-LDH	286	45	1M	[36]
$Co_{3-x}Fe_xO_4$	261	63	1M	[37]
NiCo-2.0–800HP	320	84	1M	[38]
NiCo-$NiCoO_2$@NC	318	76	1M	[39]
CoFe@N—CNTs-800	306	62	1M	[40]
CoFe-B	280	38.9	1M	[41]
a-$CoFe_2$	290	62	1M	[42]
NiCo@LDH—NC	330	36.4	1M	[43]

model, during EIS analysis performed at 1.55 V versus RHE (Figure S6, Supporting Information). From the analyses of the high-frequency semicircle (considering the same active area), RuO_2 has greater resistance (0.0421 Ω), compared to $Ni_{1-x}Co_x/NiCoO_x$, (0.0398 Ω), and $FeCo_3/FeCoO_x$ (0.0325 Ω).

It should be noted that, given the low cost of the reagents and the feasibility of the synthesis, a higher electrocatalyst loading was used for the transition metal-based nanoparticles compared to the benchmark RuO_2, considering it as a more plausible scenario from an industrial perspective. For clarity, an evaluation of the electrocatalytic activity per unit mass (mass activity) compared to geometric activity [44] is shown in Fig. 8.

3.3. AEMWE tests

To evaluate the actual applicability of the electrocatalysts obtained through the aforementioned synthetic strategy, tests were carried out in a pilot-scale AEM electrolyzer (50 cm^2) using Pt/C as a cathode electrocatalyst. Firstly, the performances were evaluated through the acquisition of polarization curves at 50 °C with KOH 1 M as supporting electrolyte Fig. 9.

As for all the electrochemical tests carried out, also the water electrolyzer tests demonstrated the higher electrocatalytic activity of the NPs here synthesized compared to the noble metal-based benchmark;

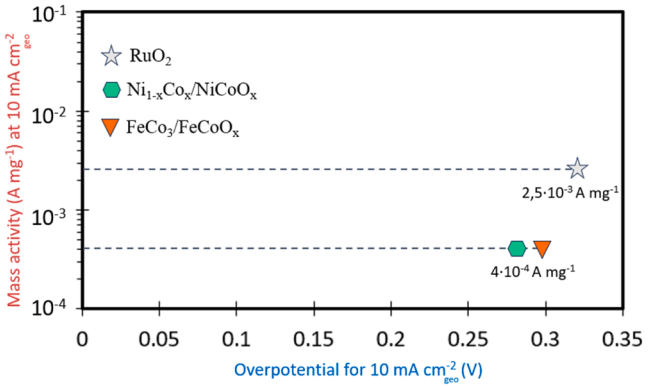

Fig. 8. Comparison of mass activity and overpotential at 10 mA cm^{-2} for OER for the developed electrocatalyst and RuO_2.

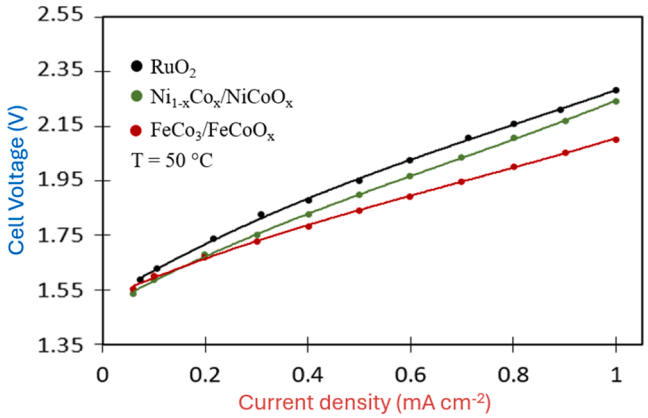

Fig. 9. Polarization curves comparison of OER electrocatalysts at 50 °C with 1.0 M KOH as supporting electrolyte: $FeCo_3/FeCoO_x$ (red curve), $Ni_{1-x}Co_x/NiCoO_x$ (green curve), RuO_2 (black curve).

with the $FeCo_3/FeCoO_x$ having higher performance than the $Ni_{1-x}Co_x/NiCoO_x$. The higher loading relative to RuO_2 offsets its greater mass activity and results in enhanced geometric activity (Fig. 8). This phenomenon is frequently reported in the literature for PGM-free electrocatalysts employed in OER [44]. In our case, this represents a satisfactory trade-off, considering the economic and practical advantages previously discussed regarding the synthetic strategy here discussed. An overview of the obtained voltages versus various current densities is given in Table 2. The voltage gap between the $FeCo_3/FeCoO_x$ and curves increases with current density, from only 7 mV at 0.2 A cm^2 up to 140 mV at 1 A cm^2, demonstrating faster kinetics at high current for the former. Consequently, the gap at 1 A cm^2 between the $FeCo_3/FeCoO_x$ and the RuO_2 is 177 mV.

Secondly, after the polarization curves, an evaluation of the degradation trend of the membrane electrode assembly (MEA) composed of $FeCo_3/FeCoO_x$ and $Ni_{1-x}Co_x/NiCoO_x$ at the anode was carried out with a continuous power supply of 0.4 A cm^2 with a supporting electrolyte (1 M KOH) temperature of 50 °C (Fig. 10). After 100 h of continuous testing, a new polarization curve was recorded and compared with the previous one (Fig. 11).

The resulting degradation rate for $FeCo_3/FeCoO_x$ was 396 mV/h (Fig. 10a) and, surprisingly, zero for $Ni_{1-x}Co_x/NiCoO_x$ (Fig. 10b) and both these trends were highlighted by the polarization curves after 100 h (Fig. 11). The second curve recorded for the $FeCo_3/FeCoO_x$ was higher with a voltage gap of 46 mV and 39 mV at 0.4 A cm^2 and 1 A cm^2 respectively compared to the first one (Fig. 11a). For $Ni_{1-x}Co_x/NiCoO_x$ the second curve is practically identical to the first up to 0.4 A cm^2 and then improves, with a vote gap at 1 A cm^2 of −94 mV (Fig. 11b). While this test was conducted on a pilot scale and offers insights into degradation trends, it should not be regarded as a conclusive endurance test from an industrial perspective, where a broader range of conditions and extended operating hours need to be considered, especially for $Ni_{1-x}Co_x/NiCoO_x$ which seems to even improve performance in the first 100 h.

Table 2
Comparison of the electrocatalytic activities in AEM cells at 50 °C.

Anode	V at 0.2 A cm^{-2}	V at 0.4 A cm^{-2}	V at 0.6 A cm^{-2}	V at 0.8 A cm^{-2}	V at 1 A cm^{-2}
RuO_2	1.731	1.878	2.022	2.162	2.279
$Ni_{1-x}Co_x/NiCoO_x$	1.678	1.826	1.966	2.105	2.242
$FeCo_3/FeCoO_x$	1.671	1.785	1.894	2.001	2.102

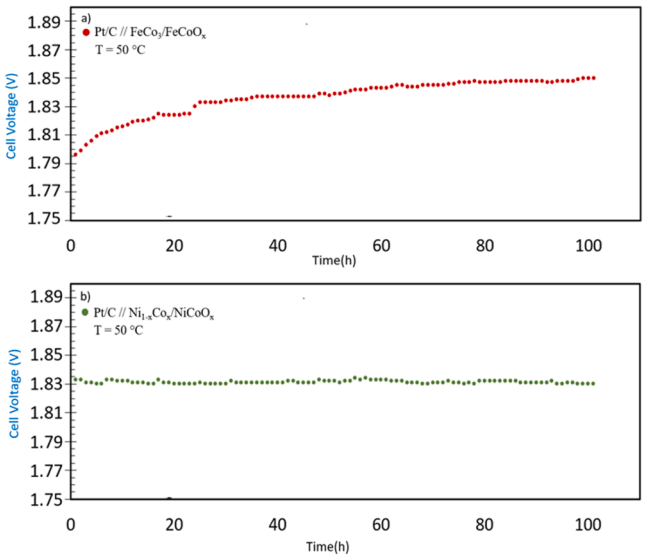

Fig. 10. Degradation trend of (a) $FeCo_3/FeCoO_x$ (red curve) MEA and (b) $Ni_{1-x}Co_x/NiCoO_x$ (green curve).

4. Perspective and outlook

According to the International Renewable Energy Agency (IRENA), achieving a significant role for green hydrogen as a low-carbon energy carrier for the energy transition will require an installed water electrolyzer capacity of 5 terawatts (TW) by 2050. To achieve such a high level of hydrogen production, priority must be given to the scaling up of low-temperature water electrolyzers, along with significant cost reductions, simplification of production processes and minimization of their environmental impact [45]. This requires the development of electrocatalysts produced via simple and scalable green synthesis methods, offering high electrocatalytic performance and durability, without relying on noble and precious metals. With this aim, this work presents a green and still little-practiced synthetic strategy to produce electrocatalysts for AEMWE; used to synthesize two different types of nanoparticles based on non-noble metals such as nickel, iron and cobalt. The synthetic strategy, common for both materials, involves two steps using water as a solvent and inexpensive, abundant, and non-toxic reagents such as aluminium powder and caustic soda. The obtained materials demonstrated higher performance in catalyzing OER compared to the noble RuO_2 in all the electrochemical tests conducted, even those in an AEMWE. The performances obtained in the AEMWE test were compared with those reported in other works, where Pt/C was used as an electrocatalyst at the cathode Table 3. Despite the already promising results, future studies will concern the tuning of the molar ratios between the metal salts used during the synthesis, not optimized here, to produce other types of alloys. Further aspects to be explored in view of a scale-up from a pilot system to an industrial one are the quantity of electrocatalyst to be applied on the electrodes and a deeper knowledge of the degradation trends.

5. Conclusions

In summary, $FeCo_3/FeCoO_x$ and $Ni_{1-x}Co_x/NiCoO_x$ nanoparticles were synthesized via a wet chemical reduction with aluminium powder. A characterization study was carried out using XRD, SEM, XPS, HR-TEM and HAADF-STEM and the electrocatalytic activity of the obtained materials for OER was evaluated by LSV, Tafel slope, EIS and AEMWE single-cell tests (using Pt/C as cathode electrocatalyst). The performances were compared with those of RuO_2, considering the mass activity and the geometrical activity. The overpotentials exhibited at a current density of 10 mA cm^{-2} in 1 M KOH were of 288 mV and 296 mV for $FeCo_3/FeCoO_x$ and $Ni_{1-x}Co_x/NiCoO_x$ respectively; outperforming the noble metal-based benchmark. This trend was maintained in the single-cell AEMWE tests as well, with the MEA with the cobalt-based anode alloy performing better (2.10 V at 1 A cm^{-2}, 50 °C) than the one with the nickel-based one (2.24 V at 1 A cm^{-2}, 50 °C). During the degradation test at a fixed current of 0.4 A cm^{-2}, the performance of the $FeCo_3/FeCoO_x$ showed a worsening of 396 μV/h while that of the $Ni_{1-x}Co_x/NiCoO_x$ remained unchanged. This was further confirmed by the polarization curves recorded after 100 h with a voltage gap at 1 A cm^{-2} between the curves of 39 mV for the former while even an improvement of - 94 mV for the latter. This study developed an effective strategy for

Table 3
MEA performance comparison.

Anode	Cathode loading (Pt/C)	Membrane	Electrolyte	V/I A cm^{-2}	T(°C)	Ref.
$Ni_{1-x}Co_x/NiCoO_x$	0.5 mg cm^{-2}	AT-100	1 M KOH	2.24/1	50	This work
$FeCo_3/FeCoO_x$	0.5 mg cm^{-2}	AT-100	1 M KOH	2.10/1	50	This work
Co_2Fe	0.25 mg cm^{-2}	FAA-3	1 M KOH	1.8/0.13	–	[46]
$Co_{1-x}Fe_x$-CNF	1 mg cm^{-2}	FAA-3–50	1 M KOH	1.7/0.794	80	[47]
CeO_2/CoFeCe-LDH	1 mg cm^{-2}	X37–50	1 M KOH	1.8/2.2	50	[48]
$Ni_{0.45}Co_{2.55}O_4$	3 mg cm^{-2}	FAA-3–50	1 M KOH	2/0.3	30	[49]
$NiCoO_x$	–	X37–50	1 M KOH	2.2/1.7	70	[50]
$NiCo_2O_4$	0.4 mg cm^{-2}	LDPE-VBC-TMA	1 M NaOH	1.95/0.42	60	[51]

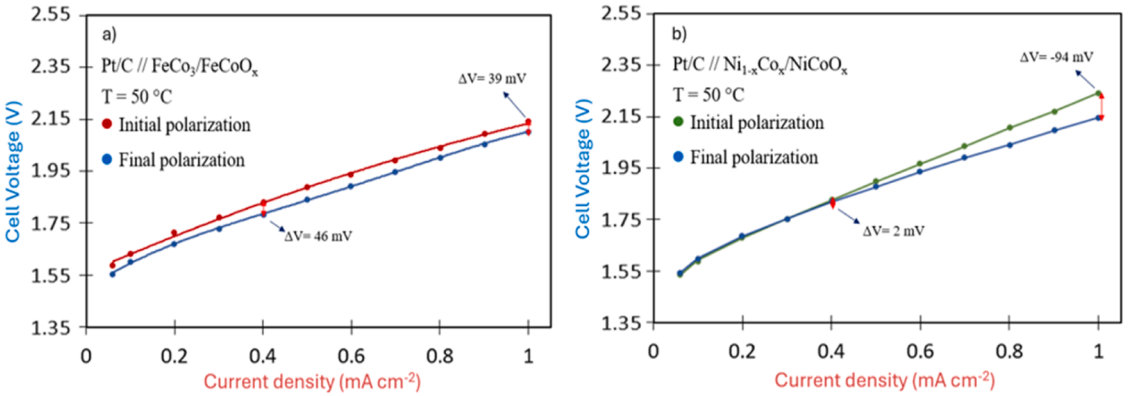

Fig. 11. AEMWE polarization curve comparison before and after 100 h of (a) $FeCo_3/FeCoO_x$ and (b) $Ni_{1-x}Co_x/NiCoO_x$.

the green synthesis of transition metal-based nanoparticles for hydrogen production in AEMWE.

CRediT authorship contribution statement

Francesko Malaj: Writing – review & editing, Writing – original draft, Visualization, Validation, Formal analysis, Data curation, Conceptualization. **Domenico Lentini:** Writing – review & editing, Writing – original draft, Visualization, Validation, Formal analysis, Conceptualization. **Alessandro Tampucci:** Methodology, Investigation, Formal analysis, Conceptualization. **Lorenzo Brogi:** Methodology, Investigation, Formal analysis. **Enrico Berretti:** Writing – original draft, Visualization, Methodology, Investigation, Formal analysis, Data curation. **Mohsin Muhyuddin:** Writing – review & editing, Writing – original draft, Methodology, Formal analysis. **Gianluigi Baiardi:** Visualization, Methodology, Investigation, Formal analysis, Data curation. **Stiven Forti:** Visualization, Methodology, Investigation, Formal analysis, Data curation. **Antonio Rossi:** Visualization, Methodology, Investigation, Formal analysis, Data curation. **Camilla Coletti:** Resources, Formal analysis, Data curation. **Oreste Tarallo:** Writing – review & editing, Writing – original draft, Supervision, Methodology, Investigation, Conceptualization. **Francesco Ruffo:** Writing – review & editing, Writing – original draft, Supervision, Conceptualization. **Carlo Santoro:** Writing – review & editing, Supervision, Project administration, Funding acquisition, Conceptualization.

Declaration of competing interest

The authors declare that they have no known competing financial interests or personal relationships that could have appeared to influence the work reported in this paper.

Supplementary materials

Supplementary material associated with this article can be found, in the online version, at doi:10.1016/j.electacta.2025.146805.

Data availability

Data will be made available on request.

References

[1] A.M. Oliveira, R.R. Beswick, Y. Yan, A green hydrogen economy for a renewable energy society, Curr. Opin. Chem. Eng. 33 (Sep. 2021) 100701, https://doi.org/10.1016/j.coche.2021.100701.

[2] A. Boretti, B.G. Pollet, Hydrogen economy: paving the path to a sustainable, low-carbon future, Int. J. Hydrog. Energy 93 (Dec. 2024) 307–319, https://doi.org/10.1016/j.ijhydene.2024.10.350.

[3] J. Chi, H. Yu, Water electrolysis based on renewable energy for hydrogen production, Chin. J. Catal. 39 (3) (Mar. 2018) 390–394, https://doi.org/10.1016/S1872-2067(17)62949-8.

[4] I. Vincent, D. Bessarabov, Low cost hydrogen production by anion exchange membrane electrolysis: a review, Renew. Sustain. Energy Rev. 81 (Jan. 2018) 1690–1704, https://doi.org/10.1016/j.rser.2017.05.258.

[5] S.A. Lee, J. Kim, K.C. Kwon, S.H. Park, H.W. Jang, Anion exchange membrane water electrolysis for sustainable large-scale hydrogen production, Carbon Neutralization 1 (1) (Jun. 2022) 26–48, https://doi.org/10.1002/cnl2.9.

[6] Z.W. Seh, J. Kibsgaard, C.F. Dickens, I. Chorkendorff, J.K. Nørskov, T.F. Jaramillo, Combining theory and experiment in electrocatalysis: insights into materials design, Science 355 (6321) (Jan. 2017) eaad4998, https://doi.org/10.1126/science.aad4998.

[7] X. Xie, et al., Oxygen evolution reaction in alkaline environment: material challenges and solutions, Adv. Funct. Mater. 32 (21) (May 2022) 2110036, https://doi.org/10.1002/adfm.202110036.

[8] F. Lu, M. Zhou, Y. Zhou, X. Zeng, First-row transition metal based catalysts for the oxygen evolution reaction under alkaline conditions: basic principles and recent advances, Small 13 (45) (Dec. 2017) 1701931, https://doi.org/10.1002/smll.201701931.

[9] G.C. Anderson, B.S. Pivovar, S.M. Alia, Establishing performance baselines for the oxygen evolution reaction in alkaline electrolytes, J. Electrochem. Soc. 167 (4) (Jan. 2020) 044503, https://doi.org/10.1149/1945-7111/ab7090.

[10] S. Park, Y. Shao, J. Liu, Y. Wang, Oxygen electrocatalysts for water electrolyzers and reversible fuel cells: status and perspective, Energy Environ. Sci. 5 (11) (2012) 9331, https://doi.org/10.1039/c2ee22554a.

[11] M. El-Shafie, Hydrogen production by water electrolysis technologies: a review, Results Eng 20 (Dec. 2023) 101426, https://doi.org/10.1016/j.rineng.2023.101426.

[12] M.-I. Jamesh, X. Sun, Recent progress on earth abundant electrocatalysts for oxygen evolution reaction (OER) in alkaline medium to achieve efficient water splitting – A review, J. Power Sources 400 (Oct. 2018) 31–68, https://doi.org/10.1016/j.jpowsour.2018.07.125.

[13] L. Trotochaud, S.L. Young, J.K. Ranney, S.W. Boettcher, Nickel–Iron oxyhydroxide oxygen-evolution electrocatalysts: the role of intentional and incidental iron incorporation, J. Am. Chem. Soc. 136 (18) (May 2014) 6744–6753, https://doi.org/10.1021/ja502379c.

[14] A. Vazhayil, L. Vazhayal, J. Thomas, S. Ashok C, N. Thomas, A comprehensive review on the recent developments in transition metal-based electrocatalysts for oxygen evolution reaction, Appl. Surf. Sci. Adv. 6 (Dec. 2021) 100184, https://doi.org/10.1016/j.apsadv.2021.100184.

[15] F. Malaj, et al., One-pot synthesis of FeNi3/FeNiOx nanoparticles for PGM-free anion exchange membrane water electrolysis, Electrochim. Acta 507 (Dec. 2024) 145109, https://doi.org/10.1016/j.electacta.2024.145109.

[16] X. Lu, et al., Ultrafast fabrication of nanospherical CoFe alloys for boosting electrocatalytic water oxidation, Int. J. Hydrog. Energy 48 (87) (Oct. 2023) 34009–34017, https://doi.org/10.1016/j.ijhydene.2023.05.105.

[17] C. Yang, et al., Scalable synthesis of bimetallic CoFe alloy nanoparticles for efficient oxygen evolution reaction, ChemistrySelect 8 (9) (Mar. 2023) e202204580, https://doi.org/10.1002/slct.202204580.

[18] B. Zhang, et al., General synthesis of NiCo alloy nanochain arrays with thin oxide coating: a highly efficient bifunctional electrocatalyst for overall water splitting, J. Alloys Compd. 797 (Aug. 2019) 1216–1223, https://doi.org/10.1016/j.jallcom.2019.05.036.

[19] S. Krishnan, et al., Current technologies for recovery of metals from industrial wastes: an overview, Environ. Technol. Innov. 22 (May 2021) 101525, https://doi.org/10.1016/j.eti.2021.101525.

[20] J. Kim, R. Kim, K.N. Han, Advances in hydrometallurgical gold recovery through cementation, adsorption, ion exchange and solvent extraction, Minerals 14 (6) (Jun. 2024) 607, https://doi.org/10.3390/min14060607.

[21] A. Maimoni, Minerals recovery from salton sea geothermal brines: a literature review and proposed cementation process, Geothermics 11 (4) (Jan. 1982) 239–258, https://doi.org/10.1016/0375-6505(82)90031-1.

[22] A.P. Reverberi, P.S. Varbanov, S. Lauciello, M. Salerno, B. Fabiano, An eco-friendly process for zerovalent bismuth nanoparticles synthesis, J. Clean. Prod. 198 (Oct. 2018) 37–45, https://doi.org/10.1016/j.jclepro.2018.07.011.

[23] R. Jhajharia, D. Jain, A. Sengar, A. Goyal, P.R. Soni, Synthesis of copper powder by mechanically activated cementation, Powder Technol 301 (Nov. 2016) 10–15, https://doi.org/10.1016/j.powtec.2016.05.031.

[24] G.D. Sulka, M. Jaskuła, Influence of the sulphuric acid concentration on the kinetics and mechanism of silver ion cementation on copper, Hydrometallurgy 77 (1–2) (Apr. 2005) 131–137, https://doi.org/10.1016/j.hydromet.2004.10.016.

[25] Z. Cheng, J. Xu, Y. Zhu, Y. Yang, F. Li, W. Chen, Synthesis of cobalt hollow spherical nanostructures using aluminum powders as reductants and templates, *J. Alloys Compd.*, 482 (1–2) (Aug. 2009) L9–L13, https://doi.org/10.1016/j.jallcom.2009.03.182.

[26] W. Li, T. Cochell, A. Manthiram, Activation of aluminum as an effective reducing agent by pitting corrosion for wet-chemical synthesis, Sci. Rep. 3 (1) (Feb. 2013) 1229, https://doi.org/10.1038/srep01229.

[27] A.H. Faqeeh, M.D. Symes, A standard electrolyzer test cell design for evaluating catalysts and cell components for anion exchange membrane water electrolysis, Electrochim. Acta 444 (Mar. 2023) 142030, https://doi.org/10.1016/j.electacta.2023.142030.

[28] E. McCafferty, Sequence of steps in the pitting of aluminum by chloride ions, Corros. Sci. 45 (7) (Jul. 2003) 1421–1438, https://doi.org/10.1016/S0010-938X(02)00231-7.

[29] J. Haber, L. Ungier, On chemical shifts of ESCA and Auger lines in cobalt oxides, J. Electron Spectrosc. Relat. Phenom. 12 (3) (Jan. 1977) 305–312, https://doi.org/10.1016/0368-2048(77)85081-0.

[30] S.P. Chenakin, N. Kruse, Surface compositional changes upon heating cobalt oxalate dihydrate in vacuum, Vacuum 187 (May 2021) 110090, https://doi.org/10.1016/j.vacuum.2021.110090.

[31] B.J. Tan, K.J. Klabunde, P.M.A. Sherwood, XPS studies of solvated metal atom dispersed (SMAD) catalysts. Evidence for layered cobalt-manganese particles on alumina and silica, J. Am. Chem. Soc. 113 (3) (Jan. 1991) 855–861, https://doi.org/10.1021/ja00003a019.

[32] S. Thoufeeq, P.K. Rastogi, S. Thomas, A. Shravani, T.N. Narayanan, M. R. Anantharaman, Single step grown NiFe sponges as efficient water splitting electrocatalysts in alkaline medium, ChemistrySelect 5 (4) (Jan. 2020) 1385–1395, https://doi.org/10.1002/slct.202000112.

[33] X. Zuo, et al., Nanostructured nickel-cobalt alloy with oxide layer for efficient oxygen evolution reaction, J. Mater. Chem. A 4 (1) (2016) 51–58, https://doi.org/10.1039/C5TA06869J.

[34] Y. Shen, et al., Prussian blue analogue-derived Ni and Co bimetallic oxide nanoplate arrays block-built from porous and hollow nanocubes for the efficient oxygen evolution reaction, Nanoscale 11 (24) (2019) 11765–11773, https://doi.org/10.1039/C9NR01804B.

[35] B. Chen, et al., One-step construction of porous Ni/Co metal/oxide nanocubes for highly efficient oxygen evolution, Electrochem. Commun. 93 (Aug. 2018) 191–196, https://doi.org/10.1016/j.elecom.2018.07.016.
[36] L. Han, et al., Dealloying-directed synthesis of efficient mesoporous CoFe-based catalysts towards the oxygen evolution reaction and overall water splitting, Nanoscale 9 (42) (2017) 16467–16475, https://doi.org/10.1039/C7NR06254K.
[37] T.H.T. Nguyen, et al., $Co_{3-x}Fe_xO_4$ inverse opals with tunable catalytic activity for high-performance overall water splitting, Nanoscale 15 (24) (2023) 10306–10318, https://doi.org/10.1039/D2NR07300E.
[38] Y. Li, J. Chen, P. Cai, Z. Wen, Tailorable nanoarchitecturing of bimetallic nickel-cobalt hydrogen phosphate via the self-weaving of nanotubes for efficient oxygen evolution, J. Mater. Chem. A 6 (12) (2018) 4948–4954, https://doi.org/10.1039/C7TA10374C.
[39] X. Zuo, et al., Bimetallic thin film NiCo-NiCoO2@NC as superior bifunctional electrocatalyst for overall water splitting in alkaline Media, J. Mater. Chem. A 4 (1) (2016) 51–58, https://doi.org/10.1039/C5TA06869J.
[40] P. Guo, et al., Multifunctional bayberry-like composites consisting of CoFe encapsulated by carbon nanotubes for overall water splitting and zinc–air batteries, J. Mater. Chem. A 9 (38) (2021) 21741–21749, https://doi.org/10.1039/D1TA06100C.
[41] C. Qiang, et al., Efficient electrocatalytic water splitting by bimetallic cobalt iron boride nanoparticles with controlled electronic structure, J. Colloid Interface Sci. 604 (Dec. 2021) 650–659, https://doi.org/10.1016/j.jcis.2021.07.024.
[42] W. Zhu, et al., Porous amorphous FeCo alloys as pre-catalysts for promoting the oxygen evolution reaction, J. Alloys Compd. 828 (Jul. 2020) 154465, https://doi.org/10.1016/j.jallcom.2020.154465.
[43] R. Patil, et al., Ultrafine bimetallic nickel–Cobalt alloy from a layered hydroxide for oxygen evolution reaction and capacitors, ACS Appl. Eng. Mater. 1 (8) (Aug. 2023) 2018–2028, https://doi.org/10.1021/acsaenm.3c00192.
[44] J. Kibsgaard, I. Chorkendorff, Considerations for the scaling-up of water splitting catalysts, Nat. Energy 4 (6) (May 2019) 430–433, https://doi.org/10.1038/s41560-019-0407-1.
[45] *Green hydrogen cost reduction: scaling up electrolysers to meet the 1.5° C climate goal.* Abu Dhabi: Irena, 2020.
[46] G.-C. Chen, T.H. Wondimu, H.-C. Huang, K.-C. Wang, C.-H. Wang, Microwave-assisted facile synthesis of cobalt iron oxide nanocomposites for oxygen production using alkaline anion exchange membrane water electrolysis, Int. J. Hydrog. Energy 44 (21) (Apr. 2019) 10174–10181, https://doi.org/10.1016/j.ijhydene.2019.02.215.
[47] S. Kang, K. Ham, J. Lee, Moderate oxophilic CoFe in carbon nanofiber for the oxygen evolution reaction in anion exchange membrane water electrolysis, Electrochim. Acta 353 (Sep. 2020) 136521, https://doi.org/10.1016/j.electacta.2020.136521.
[48] Y.S. Park, F. Liu, D. Diercks, D. Braaten, B. Liu, C. Duan, High-performance anion exchange membrane water electrolyzer enabled by highly active oxygen evolution reaction electrocatalysts: synergistic effect of doping and heterostructure, Appl. Catal. B Environ. 318 (Dec. 2022) 121824, https://doi.org/10.1016/j.apcatb.2022.121824.
[49] R.A. Murugesan, et al., Development of Ni-doped Co3O4 oxygen evolution catalysts for anion exchange membrane water electrolysis, Int. J. Hydrog. Energy 72 (Jun. 2024) 677–686, https://doi.org/10.1016/j.ijhydene.2024.05.365.
[50] K.W. Ahmed, S. Habibpour, Z. Chen, M. Fowler, Investigation of NiCoOx catalysts for anion exchange membrane water electrolysis: performance, durability, and efficiency analysis, J. Energy Storage 79 (Feb. 2024) 110149, https://doi.org/10.1016/j.est.2023.110149.
[51] C.L.I. Flores, G. Gupta, M. Mamlouk, M.D.L. Balela, Enhancing the physicochemical properties of nickel cobaltite catalyst for oxygen evolution reaction in anion exchange membrane water electrolyzers, Mater. Renew. Sustain. Energy 13 (3) (Dec. 2024) 279–290, https://doi.org/10.1007/s40243-024-00258-7.